

The Journal of the Acoustical Society of America



MAY 17 2024

Elastoacoustic wave propagation in a biphasic mechanical metamaterial^{a)} FREE

Meng Wang ; Annamaria Pau ; Marco Lepidi



J. Acoust. Soc. Am. 155, 3322–3335 (2024)

<https://doi.org/10.1121/10.0026079>



View
Online



Export
Citation

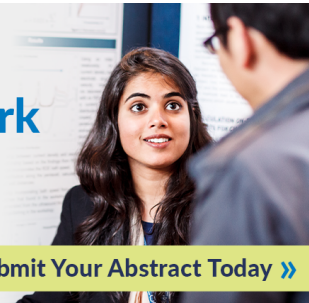


COMSOL CONFERENCE 2024 BOSTON

Showcase Your Work

Present your innovative use of modeling and simulation

Submit Your Abstract Today »



Elastoacoustic wave propagation in a biphasic mechanical metamaterial^{a)}

Meng Wang,¹  Annamaria Pau,²  and Marco Lepidi^{3,b)} 

¹Department of Astronautical, Electrical and Energy Engineering, Sapienza University of Rome, Rome, Italy

²Department of Structural and Geotechnical Engineering, Sapienza University of Rome, Rome, Italy

³Department of Civil, Chemical and Environmental Engineering, University of Genoa, Genoa, Italy

ABSTRACT:

Humans are sensitive to air-borne sound as well as to mechanical vibrations propagating in solids in the frequency range below 20 kHz. Therefore, the development of multifunctional filters for both vibration reduction and sound insulation within the frequency range of human sensitivity is a research topic of primary interest. In this paper, a high-contrast biphasic mechanical metamaterial, composed of periodic elastic solid cells with air-filled voids, is presented. By opening intercellular air-communicating channels and introducing channel-bridging solid-solid couplings, the frequency dispersion spectrum of the metamaterial can be modified to achieve complete and large bandgaps for acoustic and elastic waves. From a methodological viewpoint, the eigenproblem governing the free wave propagation is solved using a hybrid analytical-computational technique, while the waveform classification is based on polarization factors expressing the fraction of kinetic and elastic energies stored in the solid and fluid phases. Based on these theoretical results, a mechanical metafilter consisting of an array of a finite number of metamaterial cells is conceived to provide a technical solution for engineering applications. The forced response of the metafilter is virtually tested in a computational framework to assess its performance in passively controlling the propagation of broadband sound and vibration signals within solid and fluid environments. Quantitative results synthesized by transmission coefficients demonstrate that the metafilter can remarkably reduce the transmitted response in the frequency band of human sensitivity. © 2024 Acoustical Society of America. <https://doi.org/10.1121/10.0026079>

(Received 18 January 2024; revised 6 April 2024; accepted 3 May 2024; published online 17 May 2024)

[Editor: Vladislav Sergeevich Sorokin]

Pages: 3322–3335

I. INTRODUCTION

Phononic crystals are artificial composite media geometrically characterized by a periodic distribution of elementary units, blocks, or cells (Laude, 2020; McGurn, 2022). At the macroscopic level, the dynamical free and forced response is determined by the mechanical parameters of the ingredient materials, as well as by the microstructural properties characterizing the cellular compositeness, architecture, and topology (Hussein *et al.*, 2014; Maldovan, 2013). Consequently, the recent extraordinary developments in the complementary fields of theoretical formulations, virtual simulations, microengineering technologies, parametric design, and holonic manufacturing pave the way for launching a new generation of functional materials and metamaterials with finely tunable or customizable acoustic and elastic performances (Romero-García *et al.*, 2009; Wang *et al.*, 2020a). Specifically, a fundamental functionality of theoretical and applied interest is the tailored inhibition of wave propagation within certain target ranges of frequencies (Chen *et al.*, 2022; Cummer *et al.*, 2016; Martínez-Sala *et al.*, 1995; Oudich *et al.*, 2023). In this respect, multi-

phasic phononic crystals can exhibit high contrasts among the mechanical parameters of the constituent phases (Tanaka *et al.*, 2000). Therefore, strong or even extreme modulations of the constitutive properties can be achieved, without violating the crystal periodicity. Remarkably—from the perspective of inverse problems—the interphasic mechanical mismatches can be regarded as design variables with large admissible domains of variability. The consequent rich designability opens the possibility of passively controlling the natural dispersion relations of the phononic crystal to filter out the frequency bands of sounds (acoustic phononic crystals) and/or vibrations (elastic phononic crystals). Following this general idea, phononic filters can be successfully employed as silencers and/or isolators, respectively, in a variety of traditional and emerging engineering applications (Delpero *et al.*, 2016; Gao *et al.*, 2022; Krushynska *et al.*, 2023).

Harmonic wave propagation in non-dissipative dispersive media is naturally inhibited in all the frequency ranges corresponding to stopbands (or bandgaps) in the dispersion spectrum. Particularly, acoustic bandgaps refer conventionally to stopbands centered in the frequency range of pressure waves propagating within a fluid, while elastic bandgaps refer to stopbands centered in the frequency range of pressure/shear waves propagating within a solid medium (Goffaux and Vigneron, 2001; Sigalas, 1992). Typically,

^{a)}This paper is part of a special issue on Wave phenomena in periodic, near-periodic, and locally resonant systems.

^{b)}Email: marco.lepidi@unige.it

bandgap formation can be attributed to physical effects like Bragg scattering or Fano resonance. The former effect originates from the destructive interference of harmonic waves propagating through periodic crystal lattices at wavelengths comparable (in magnitude) to the interdistance among the crystal atoms (lattice constants). The latter effect originates from the introduction of discrete or local tunable resonators, technically realizable as intracellular auxiliary oscillators, generating frequency veering phenomena in the dispersion spectrum by virtue of internal resonance mechanisms (Liu *et al.*, 2000; Zangeneh-Nejad and Fleury, 2019).

The growing possibilities of integrating locally resonating micromechanisms at unprecedented subwavelength scales—by virtue of high-precision microprinting and micromachining—has enormously enlarged the targetable frequency ranges of spectral design (Gao *et al.*, 2023; Li *et al.*, 2021; Ma and Sheng, 2016; Zega *et al.*, 2022). The enlarged space of inverse problem solutions for locally resonating microstructures is further enriched by the high sensitivity shown by waveforms and other spectral properties, like polarization factors, group velocities, and energy fluxes, to the microstructural design variables (Bacigalupo and Lepidi, 2018; Lepidi and Bacigalupo, 2018). The consequent capacity of phononic crystals and mechanical metamaterials to passively control the propagation of elastic and acoustic waves has given rise to numerous applications, including noise silencing (Vasseur *et al.*, 2002; Zhao *et al.*, 2010), vibration damping (Frazier and Hussein, 2015; Hussein and Frazier, 2010), nonreciprocal uni-directional waveguiding (Chen *et al.*, 2017; Patil *et al.*, 2022). Within this vibrating and rapidly developing research framework, the challenge of conceiving, modeling, analyzing, and designing artificial systems capable of simultaneously dampening sound and vibration remains an ongoing endeavor worth investigation (Zangeneh-Nejad and Fleury, 2019; Zhang *et al.*, 2023). Furthermore, the recent advent of modern methods of machine learning, evolutionary algorithms, and other metaheuristic procedures has provided further impetus to maximizing metamaterial performances through multi-objective optimization techniques (Bacigalupo *et al.*, 2021; Bilal and Hussein, 2011; D'Alessandro *et al.*, 2018).

Conventional approaches for vibro-acoustic attenuation exploit the acoustic mass law or the introduction of an absorbing layer to maximize the transmission loss. The former approach tends to considerably increase inertias and weights, which are mass-proportional properties. The latter usually implies thick stratifications, since absorbing layers are required to have thicknesses comparable with the acoustic wavelengths. These physical shortcomings may limit the applicability of traditional solutions for low-frequency attenuation of acoustic and elastic waves in lightweight applications (Claeys *et al.*, 2013). Nonetheless, investigations focused on alternative approaches based on high-contrast biphasic (solid-fluid) phononic crystals and metamaterials are relatively recent (Bilal *et al.*, 2018; Elmadih *et al.*, 2021; Jiang and Chen, 2019), but remain rather limited. In this respect, it can be remarked that, on the one hand, the governing equations characterized by

high-contrasting coefficients in the multi-phasic cellular domain require advanced methodological tools of analytical and numerical solution (Hou *et al.*, 2006; Li *et al.*, 2018, 2011). Particularly, the consistent statement and treatment of the coupled equations governing the kinematic continuity and dynamic equilibrium at the solid-fluid interfaces is a crucial issue to correctly assess the elastoacoustic band structure of multi-phasic phononic crystals. However, on the other hand, the interplay between elastic and acoustic waves generates a rich scenario of spectral interactions and coupling phenomena (Wang *et al.*, 2020b), deserving to be investigated and suitable to be harnessed for functional purposes. Therefore, several fascinating scientific and technological challenges remain open, and much space remains to explore the limitless possibilities of novel typological and topological solutions.

Within this motivating background, the present work investigates the free and forced dynamic response of a periodic biphasic metamaterial, with the primary objective of achieving a significant reduction of both acoustic and elastic wave transmission. Target frequency bands to be filtered fall into the human sensitivity range to airborne sounds and mechanical vibrations. First, the mechanical biphasic metamaterial is described, and then its dispersion properties are determined (Sec. II). Based on the encouraging theoretical results, a low-dimension metafilter is proposed and virtually tested to assess its performance in preventing the transmission of broadband excitations propagating in fluid and solid environments (Sec. III). From the methodological viewpoint, the spectral analyses are pursued by an extension of the semi-analytical finite element technique to a classical continuum, combined with energy-based factors describing the waveform polarization. The performances of the mechanical metafilter are instead quantitatively evaluated by means of transmission coefficients, accounting for the ratio between forced response to broadband excitations in the presence and in the absence of the metafilter.

II. TWO-DIMENSIONAL (2D) BIPHASIC MECHANICAL METAMATERIAL

A 2D phononic crystal generated by the infinite periodic repetition of a square centrosymmetric cell is considered (Fig. 1). The spatial repetitiveness of the cellular pattern is fully characterized by a pair of orthogonal periodicity vectors \mathbf{a}_1 and \mathbf{a}_2 . The periodic cell is characterized by a high-contrast biphasic topology [Fig. 2(a)], in which centered circular interfaces separate the solid matrix (phase I, gray regions) from the fluid filler (phase II, light blue regions). This native topology can be enriched with micro-structurization to transform the phononic crystal into a highly functionalizable mechanical metamaterial, or metaplate, without altering the original periodicity. Specifically, straight inter-cellular channels, collinear to the periodicity vectors, are opened to connect the fluid phases of each pair of adjacent cells. Moreover, the separated solid parts of each cell are connected to remotely interact with each other. Such solid-solid interactions consist of linear elastic coupling

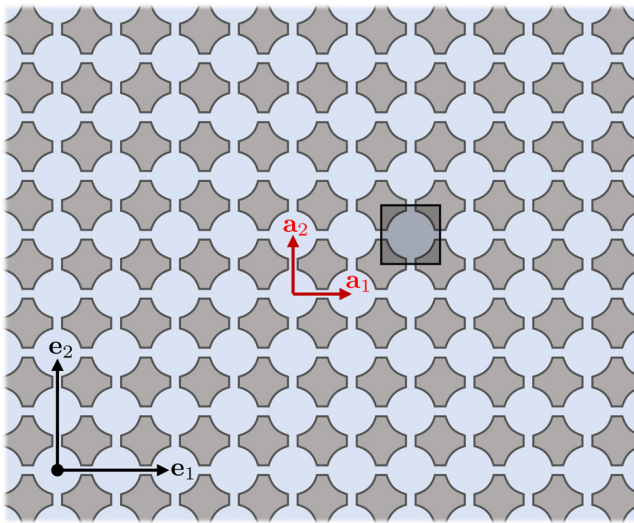


FIG. 1. (Color online) 2D biphasic mechanical metamaterial: periodic pattern and periodicity vectors.

generating repulsion and attraction forces exchanged across the channels, and are here simulated by spring beds, with total stiffness κ . The geometry of the phononic crystal is fully characterized by the cell side length $L = |\mathbf{a}_1| = |\mathbf{a}_2|$, the circular interface radius r , and the channel width w .

A. Governing equations

The dynamic configuration of the biphasic mechanical metamaterial is characterized by a plane state of strain, described by the displacement vector field $\mathbf{u} = (u_1, u_2)^\top$, which is an unknown function of time t and position vector $\mathbf{x} = (x_1, x_2)^\top$, spanning the plane defined by the two orthonormal vectors $\mathbf{e}_1 - \mathbf{e}_2$. The solid phase I is made of a non-dissipative, linearly elastic, homogeneous, and isotropic continuum. In the absence of forces other than inertia, the field equations governing the free undamped dynamics in the solid domain are

$$\mu\Delta\mathbf{u} + (\lambda + \mu)\nabla\text{div}\mathbf{u} = \rho_S\ddot{\mathbf{u}}, \quad (1)$$

where ρ_S is the solid mass density, λ and μ are the Lamé constants, $\nabla = \partial/\partial\mathbf{x}$ and $\Delta = \nabla \cdot \nabla$ are partial differential

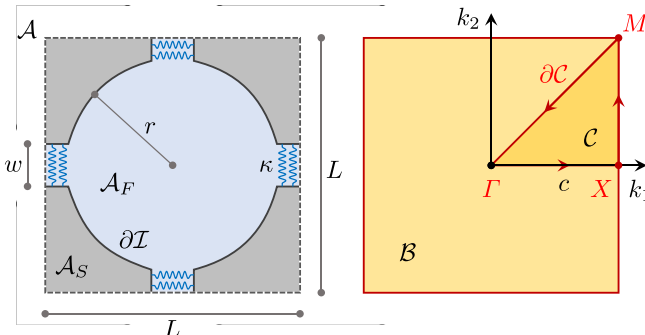


FIG. 2. (Color online) Periodic square cell of the mechanical metamaterial: (a) biphasic topology, (b) first Brillouin zone.

operators with respect to space, while overdot indicates partial differentiation with respect to time.

The fluid phase II is made of a nonviscous, nondissipative, elastically compressible homogeneous continuum. The field equations governing the free undamped dynamics in the fluid domain are

$$c_F^2\nabla(\text{div}\mathbf{u}) = \ddot{\mathbf{u}}, \quad (2)$$

where $c_F^2 = B/\rho_F$ is the square velocity of sound in the fluid, which depends on the compressibility coefficient B and the fluid mass density ρ_F . The fluid is assumed to be irrotational, that is, the rotor of the velocity field is null. This assumption results in the equality $\partial\dot{u}_1/\partial x_2 = \partial\dot{u}_2/\partial x_1$. The fluid pressure $p = B\nabla\mathbf{u}$ is a secondary \mathbf{u} -dependent variable of interest. The field equations are complemented by boundary conditions at the interface $\partial\mathcal{I}$ between the solid and the fluid domains, expressing continuity of displacements and balance of normal tractions. The tangential component of tractions on the interface is set to zero.

B. Solution methodology

Free dynamic solutions are sought in the form of periodic waves, harmonically oscillating in time with real-valued circular frequency ω while periodically propagating in space with a plane wavefront orthogonal to the real-valued wavevector $\mathbf{k} = (k_1, k_2)^\top$. Accordingly, the tentative solution can be expressed as

$$\mathbf{u}(\mathbf{x}, t) = \mathbf{U}(\mathbf{x})e^{i(\mathbf{k}\cdot\mathbf{x}-\omega t)}, \quad (3)$$

where the vector field $\mathbf{U}(\mathbf{x}) = (U_1, U_2)^\top$ plays the role of time-independent waveform, depending parametrically on the wavevector. It should be noted that the solution in Eq. (3) is enforced both in the solid and in the fluid phase. In this way, for harmonic waves, the condition of irrotational fluid results in a condition onto the derivatives of the displacement field, that is: $\partial u_1/\partial x_2 = \partial u_2/\partial x_1$.

From the methodological viewpoint, solutions are determined by a hybrid analytical-computational technique (Pau and Lanza Di Scalea, 2015) which is an extension of the classical Semi-Analytical Finite Element Method (SAFE). SAFE was initially formulated to compute the dispersion relation in guided waves (Marzani *et al.*, 2008). It should be mentioned that other approaches to the modelling and analysis of periodic materials, including homogenization into high order and multifield continua (Faraci *et al.*, 2022; Pau and Trovalusci, 2021; Sharma *et al.*, 2017), are viable. By substituting the solution from Eq. (3) into Eqs. (1) and (2), a linear ordinary differential eigenvalue problem (precisely a regular Sturm-Liouville eigenproblem) can be stated. In the solid phase, the eigenproblem is governed by equations

$$\begin{aligned} &(\lambda + 2\mu)(U_{1,11} + 2ik_1 U_{1,1} - k_1^2 U_1) \\ &+ \lambda(U_{2,21} + ik_2 U_{2,1} + ik_1 U_{2,2} - k_1 k_2 U_2) \\ &+ \mu(U_{1,22} + 2ik_2 U_{1,2} - k_2^2 U_1 + U_{2,12} \\ &+ ik_1 U_{2,2} + ik_2 U_{2,1} - k_1 k_2 U_2) = -\omega^2 U_1, \end{aligned} \quad (4)$$

$$\begin{aligned} & (\lambda + 2\mu)(U_{2,22} + 2ik_2 U_{2,2} - k_2^2 U_2) \\ & + \lambda(U_{1,12} + ik_1 U_{1,2} + ik_2 U_{1,1} - k_1 k_2 U_1) \\ & + \mu(U_{1,21} + 2ik_1 U_{2,1} - k_1^2 U_2 + U_{1,12} \\ & + ik_2 U_{1,1} + ik_1 U_{1,2} - k_1 k_2 U_1) = -\omega^2 U_2, \end{aligned} \quad (5)$$

where subscript $j = 1, 2$ after comma indicates partial differentiation $\partial/\partial x_j$. In the complementary fluid phase, the eigenproblem is governed by equations

$$\begin{aligned} c_F^2 U_{1,11} + ic_F^2(k_1 U_{1,1} + k_2 U_{1,2}) - c_F^2(k_1^2 + k_2^2) U_1 \\ = -\omega^2 U_1, \end{aligned} \quad (6)$$

$$\begin{aligned} c_F^2 U_{2,22} + ic_F^2(k_1 U_{2,1} + k_2 U_{2,2}) - c_F^2(k_1^2 + k_2^2) U_2 \\ = -\omega^2 U_2, \end{aligned} \quad (7)$$

with boundary conditions imposing the continuity of displacements, the balance of normal tractions, and the nullity of tangential tractions at the interfaces between the two phases. The square of the frequency ω^2 and the vector field $\mathbf{U}(\mathbf{x})$ play the role of unknown eigenvalue and eigenfunction, respectively. It should be noticed that, given the form of the tentative solution from Eq. (3), the eigenfunctions are complex-valued in the general case. Eigenvalues and eigenfunctions are both parameterized with respect to the varying real-valued wavevector \mathbf{k} , according to the so-called *inverse method* of solution (Hussein *et al.*, 2014).

Calling for Floquet boundary conditions, where no assumed displacement solution is used, corresponds to the enforcing of periodicity of the assumed solution of the SAFE technique, in terms of solutions of the eigenproblem (Hakoda *et al.*, 2018). Therefore, for the particular topology under investigation, the periodicity can be imposed directly on the waveform $\mathbf{U}(\mathbf{x})$, by assuming

$$\mathbf{U}(\mathbf{x}) = \mathbf{U}(\mathbf{x} + \mathbf{a}_1), \quad \mathbf{U}(\mathbf{x}) = \mathbf{U}(\mathbf{x} + \mathbf{a}_2), \quad (8)$$

$$\nabla \mathbf{U}(\mathbf{x}) = \nabla \mathbf{U}(\mathbf{x} + \mathbf{a}_1), \quad \nabla \mathbf{U}(\mathbf{x}) = \nabla \mathbf{U}(\mathbf{x} + \mathbf{a}_2), \quad (9)$$

and, consequently, the eigenproblem can be solved within the finite cellular domain $\mathcal{A} = \{\mathbf{x} : \mathbf{x} \in [-L/2, L/2] \times [-L/2, L/2]\}$ of the periodic cell, whereas the wavevector \mathbf{k} spans the square first Brillouin zone $\mathcal{B} = \{\mathbf{k} : \mathbf{k} \in [-\pi/L, \pi/L] \times [-\pi/L, \pi/L]\}$, as illustrated in Fig. 2. The cellular domain can be regarded as the union $\mathcal{A} = \mathcal{A}_S \cup \mathcal{A}_F$ of the solid phase domain \mathcal{A}_S and the fluid phase domain \mathcal{A}_F .

C. Dispersion properties

The dispersion properties that fully characterize the free wave propagation of harmonic waves in the mechanical metamaterial consist of the infinite eigenpairs (ω, \mathbf{U}) , determined as multivalued functions $\omega(\mathbf{k})$ and $\mathbf{U}(\mathbf{k})$ of the variable wavevector $\mathbf{k} \in \mathcal{B}$. Physically, each eigenpair corresponds to a different periodic wave that harmonically oscillates in time with circular frequency $\omega(\mathbf{k})$ and waveform $\mathbf{U}(\mathbf{k})$, while freely propagating

in space with wavevector \mathbf{k} . The vector quantity $\mathbf{v}(\mathbf{k}) = \nabla_{\mathbf{k}}\omega(\mathbf{k})$ indicates the directional group velocity.

From the computational viewpoint, the multi-valued frequency dispersion relation $f(\mathbf{k}) = \omega(\mathbf{k})/(2\pi)$ can be determined numerically by repeatedly solving the governing eigenproblem over a sufficiently fine discretization of the 2D Brillouin zone \mathcal{B} . As a convenient cost-saving alternative, the analysis can be limited to the Irreducible Brillouin Contour, that is the closed boundary $\partial\mathcal{C}$ of the triangular Irreducible Brillouin Zone $\mathcal{C} \subset \mathcal{B}$ identified by the three vertices $\Gamma = (0, 0)$, $X = (\pi/L, 0)$, $M = (\pi/L, \pi/L)$. The closed boundary $\partial\mathcal{C}$ is spanned by the curvilinear abscissa $c \in [0, (2 + \sqrt{2})\pi/L]$, known as *reduced wavevector*. The *dispersion curves*, or *branches*, mapping the dispersion relation $f(c) = \omega(c)/(2\pi)$ define the spectral diagram or frequency *band structure* of the metamaterial. Physically, all the frequency ranges included in the real-valued codomain of the multi-valued function $f(\mathbf{k})$, or $f(c)$, correspond to *passbands*, in which harmonic waves can freely propagate. Complementarily, frequency ranges excluded from the real-valued codomain of the multivalued function $f(\mathbf{k})$, or $f(c)$, correspond to *complete stopbands* or *bandgaps*, in which propagation of harmonic waves is inhibited for each wavevector. It may be worth noting that the completeness of the dispersion property description in terms of band structure is guaranteed by their values attained over $\partial\mathcal{C}$, at least in a statistical sense (Maurin *et al.*, 2018).

The dispersion diagrams corresponding to a particular mechanical metamaterial are exemplified in Fig. 3, with a focus on the frequency range of human sensitivity (namely, below 25 kHz). The geometrical parameters of the periodic cell and the mechanical properties of the two phases are listed in Table I. The governing eigenproblem is solved by the finite element method, using 2D second order triangular Lagrangian elements to discretize the cell domain. The maximum finite element size is not larger than 1/6 of the shortest wavelength of interest, that is 5 mm. The finite element problem is solved by using the software COMSOL in PDE mode, for both the eigenproblem and the time step analyses. In the absence of inter-cellular channels [Fig. 3(a)], the metamaterial presents the typical spectral features of a dispersive fluid-filled biphasic phononic crystal, that is (i) a triplet of low-frequency dispersion curves showing a strong nonlinear dependence on the reduced wavevector c , two of which attain zero frequency ($f=0$) at the limit of long wavelengths (Γ -vertex at $\mathbf{k} = \mathbf{0}$, or $c = 0$), and (ii) many flat bands exhibiting nearly c -independent frequencies (Laude, 2020). It should be noticed that the triplet of dispersion curves determines a low-frequency passband (green band), whose bandwidth $A_P \simeq 18$ kHz covers almost 70% of the frequency range of interest. In addition, a unique complete bandgap occurs in the high-frequency range (red band), with a narrow bandwidth $A_S \simeq 2$ kHz and center frequency $f_S \simeq 20$ kHz.

The opening of the inter-cellular channels [Fig. 3(b)] determines a drastic change in the dispersion diagram. On the one hand, the triplet of dispersion curves persists but

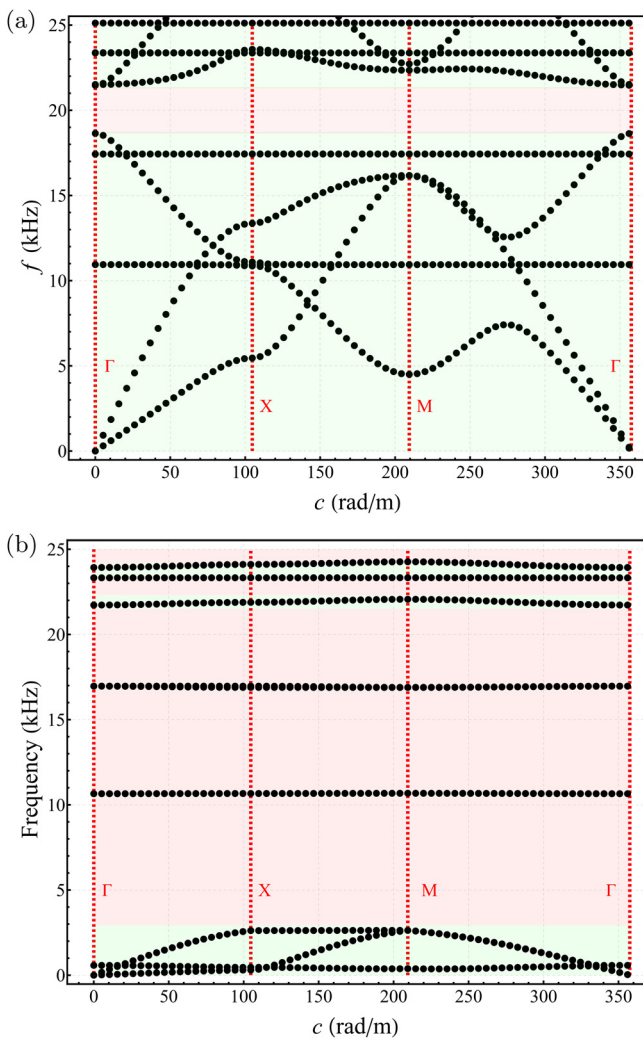


FIG. 3. (Color online) Dispersion diagrams of the biphasic mechanical metamaterial: (a) solid cell with fluid void and (b) with channels.

covers a remarkably lower range of frequencies. This corresponds to a pass bandwidth $A_P \simeq 3$ kHz that covers less than 15% of the frequency range of interest (green band). On the other hand, the remaining part of the frequency range of interest is covered by large bandgaps (red bands), interrupted only by a few flat or quasi-flat bands with negligible bandwidths.

1. Waveform classification

Determining whether the pass/stop bands enable/disable the free propagation of acoustic and/or elastic excitations is a matter involving not only the frequency ranges but also the nature of the waveforms, which can be more or less

TABLE I. Geometrical properties of the periodic cell and mechanical properties of the solid phase (nylon) and fluid phase (air).

L	r	w	ρ_S	λ	μ	ρ_F	c_F	B	κ
mm	mm	mm	kg/m ³	GPa	GPa	kg/m ³	m/s	kPa	N/m
30	12	6	1000	1.277	0.658	1.02	343	101	1.48×10^7

orthogonal to an external excitation (Laude, 2020). To this specific purpose, waveform classification can be based on elastic wave polarization (Bacigalupo and Lepidi, 2018), which is a concept borrowed from the theory of electromagnetism. Specifically, the total kinetic energy associated with a certain harmonic wave freely propagating at a frequency $\omega(\mathbf{k})$ through the biphasic metamaterial is $T(\mathbf{k}) = T_S(\mathbf{k}) + T_F(\mathbf{k})$, where

$$T_S(\mathbf{k}) = \frac{1}{4} \omega(\mathbf{k})^2 \int_{A_S} \rho_S \bar{\mathbf{U}}(\mathbf{k}) \cdot \mathbf{U}(\mathbf{k}) d\mathbf{x}, \quad (10)$$

$$T_F(\mathbf{k}) = \frac{1}{4} \omega(\mathbf{k})^2 \int_{A_F} \rho_F \bar{\mathbf{U}}(\mathbf{k}) \cdot \mathbf{U}(\mathbf{k}) d\mathbf{x} \quad (11)$$

are the kinetic energies stored, respectively, in the solid and fluid phases. The overbar stands for complex conjugate. Accordingly, an energy-based *polarization factor* can be defined as

$$\Lambda_S(\mathbf{k}) = \frac{T_S(\mathbf{k})}{T_S(\mathbf{k}) + T_F(\mathbf{k})} \quad (12)$$

to express the fraction of the total kinetic energy stored in the solid phase. According to its definition and interpretation, the polarization factor is conceptually analogous to energy-based factors used to study modal localization and hybridization (Gattulli and Lepidi, 2007).

From the mathematical viewpoint, the polarization factor can be regarded as a secondary dispersion variable, depending on the waveform $\mathbf{U}(\mathbf{k})$ and—in principle—can attain all the real values in the range [0, 1]. From the mechanical viewpoint, waves perfectly localized in the solid phase have unitary polarization factor $\Lambda_S(\mathbf{k})$. Conversely, waves perfectly localized in the fluid phase have null polarization factor $\Lambda_S(\mathbf{k})$. The fraction of the total kinetic energy stored in the fluid phase is expressed by the complementary polarization factor $\Lambda_F(\mathbf{k}) = 1 - \Lambda_S(\mathbf{k})$. Clearly, polarization factors close to unity correspond to nearly-polarized solid waves [referred to as *elastic waves* for $\Lambda_S(\mathbf{k}) \simeq 1$] or nearly-polarized fluid waves [referred to as *acoustic waves* for $\Lambda_F(\mathbf{k}) \simeq 1$].

Polarization factors enable one to qualitatively and quantitatively classify the waveforms associated with different branches of the dispersion diagram for a given wavevector, as well as to track the polarization evolution of an individual waveform under varying wavevectors. To exemplify, the lowest six frequencies of the dispersion diagram and the related waveforms associated with a particular value $c = 26.18$ rad/m of the reduced wavevector have been selected (Fig. 4). Their frequencies are listed in Table II, and their waveforms are illustrated in Fig. 5, respectively. The three frequencies $f_S^I, f_S^{II}, f_S^{III}$ extracted from the triplet of low-frequency dispersion curves are associated with elastic waveforms strongly polarized in the solid phase (with $\Lambda_S > 0.99$). On the contrary, each of the three multiple frequencies $f_F^I, f_F^{II}, f_F^{III}$ extracted from high-frequency flat dispersion curves are associated with two (f_F^I, f_F^{III}) or four (f_F^{II})

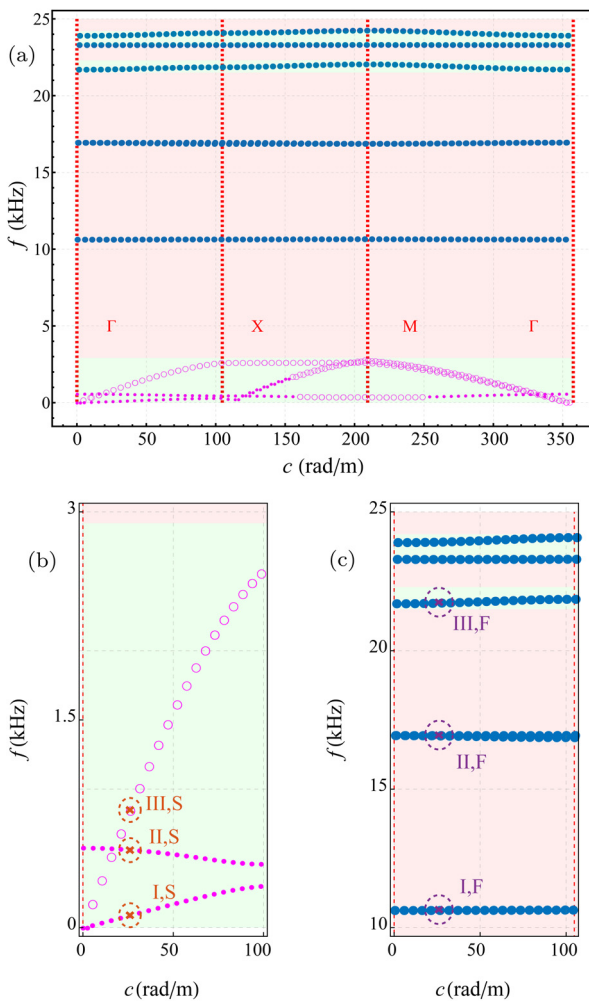


FIG. 4. (Color online) Dispersion properties: (a) dispersion diagram with distinction of frequency curves associated with acoustic waveforms (blue dots), elastic shear waveforms (purple dots), elastic pressure waveforms (purple circles); (b), (c) selection of lowest frequencies for reduced wavevector $c = 26.18 \text{ rad/m}$.

acoustic waveforms strongly polarized in the fluid phase (with $A_S < 0.01$). In particular, Fig. 5 reports the contour plots over the deformed shape of the modulus of the displacement vector field for the elastic waveforms (left) and the acoustic waveforms (right). It can be seen that, as frequency increases, the acoustic waveforms present more and more crests, or local maxima, in the displacement field, in an analogy with the sequence of natural modes in a mechanical system. Comprehensive analyses of the polarization factors, here not reported for the sake of brevity, enable one to extend the waveform classification and discriminate

TABLE II. Selection of dispersion properties: lowest frequencies at the reduced wavevector $c = 26.18 \text{ rad/m}$.

Solid	Fluid
f_S^I	0.11 kHz
f_S^{II}	0.56 kHz
f_S^{III}	0.85 kHz
	f_F^I
	f_F^{II}
	f_F^{III}
	10.65 kHz
	16.97 kHz
	21.75 kHz

between elastic low-frequency curves (purple dots and purple circles $A_S > 0.90$) and acoustic high-frequency curves (blue dots $A_S < 0.10$) of Figs. 4(a)–4(c). It was found that waveforms tend to be strongly polarized. This can be attributed to the high contrast between the mechanical properties of the two phases. In addition, it should be noted that the waveforms associated with the frequencies belonging to flatbands are quasi c -independent.

For elastic waves, an interesting subclassification can be introduced to distinguish mostly-pressure and mostly-shear waves polarized in the solid phase (Hagedorn and DasGupta, 2007). The distinction can be pursued by defining a *polarization subfactor* based on the elastic strain energy. Specifically, the elastic energy stored in the solid phase for a certain harmonic wave can be expressed as the sum $E_S(\mathbf{k}) = E_{SS}(\mathbf{k}) + E_{SP}(\mathbf{k})$, where

$$E_{SS}(\mathbf{k}) = \frac{1}{4} \int_{A_S} \mu (\overline{U}_{2,1}(\mathbf{k}) + \overline{U}_{1,2}(\mathbf{k})) (U_{2,1}(\mathbf{k}) + U_{1,2}(\mathbf{k})) d\mathbf{x} \quad (13)$$

is the portion of elastic energy associated with shear strains, while

$$E_{SP}(\mathbf{k}) = \frac{1}{4} \int_{A_S} [((\lambda + 2\mu) \overline{U}_{1,1}(\mathbf{k}) + \lambda \overline{U}_{2,2}(\mathbf{k})) U_{1,1} + ((\lambda + 2\mu) \overline{U}_{2,2}(\mathbf{k}) + \lambda \overline{U}_{1,1}(\mathbf{k})) U_{2,2}] d\mathbf{x} \quad (14)$$

is the complementary portion related to normal strains.

Focusing on the elastic energy associated with shear strains, the *polarization subfactor* can be defined

$$\Lambda_{SS}(\mathbf{k}) = \frac{E_{SS}(\mathbf{k})}{E_{SS}(\mathbf{k}) + E_{SP}(\mathbf{k})} = \frac{E_{SS}(\mathbf{k})}{A_S(\mathbf{k}) T(\mathbf{k})}, \quad (15)$$

where the energy relation $E_S(\mathbf{k}) = T_S(\mathbf{k})$, valid for harmonic waves, has been used. The subfactor $\Lambda_{SS}(\mathbf{k})$ mathematically expresses the fraction of elastic energy associated with shear strains. The fraction of elastic energy associated with normal strains is expressed by the complementary subfactor $\Lambda_{SP}(\mathbf{k}) = 1 - \Lambda_{SS}(\mathbf{k})$. From a mechanical viewpoint, elastic waves dominated by normal strains have null or quasi-null polarization subfactor ($\Lambda_{SS}(\mathbf{k}) \approx 0$) and can be classified as *pressure waves*, or *longitudinal waves*. Conversely, elastic waves dominated by shear strains have unitary or quasi-unitary polarization subfactor ($\Lambda_{SS}(\mathbf{k}) \approx 1$) and can be classified as *shear waves*, or *transversal waves*.

By applying the polarization-based subclassification to the waveforms at frequencies $f_S^I-f_S^{II}-f_S^{III}$, a shear-polarization with $\Lambda_{SS} > 0.80$ can be observed for the first two waveforms and a pressure-polarization with $\Lambda_{SS} \approx 0.20$ for the third waveform. By extending the polarization-based classification, pressure waves (fuchsia circles) and shear waves (purple dots) are found to co-exist in the low-frequency triplet of dispersion curves, as shown in Fig. 4(b). In addition, the detail of Fig. 4(b) shows that the dispersion curves

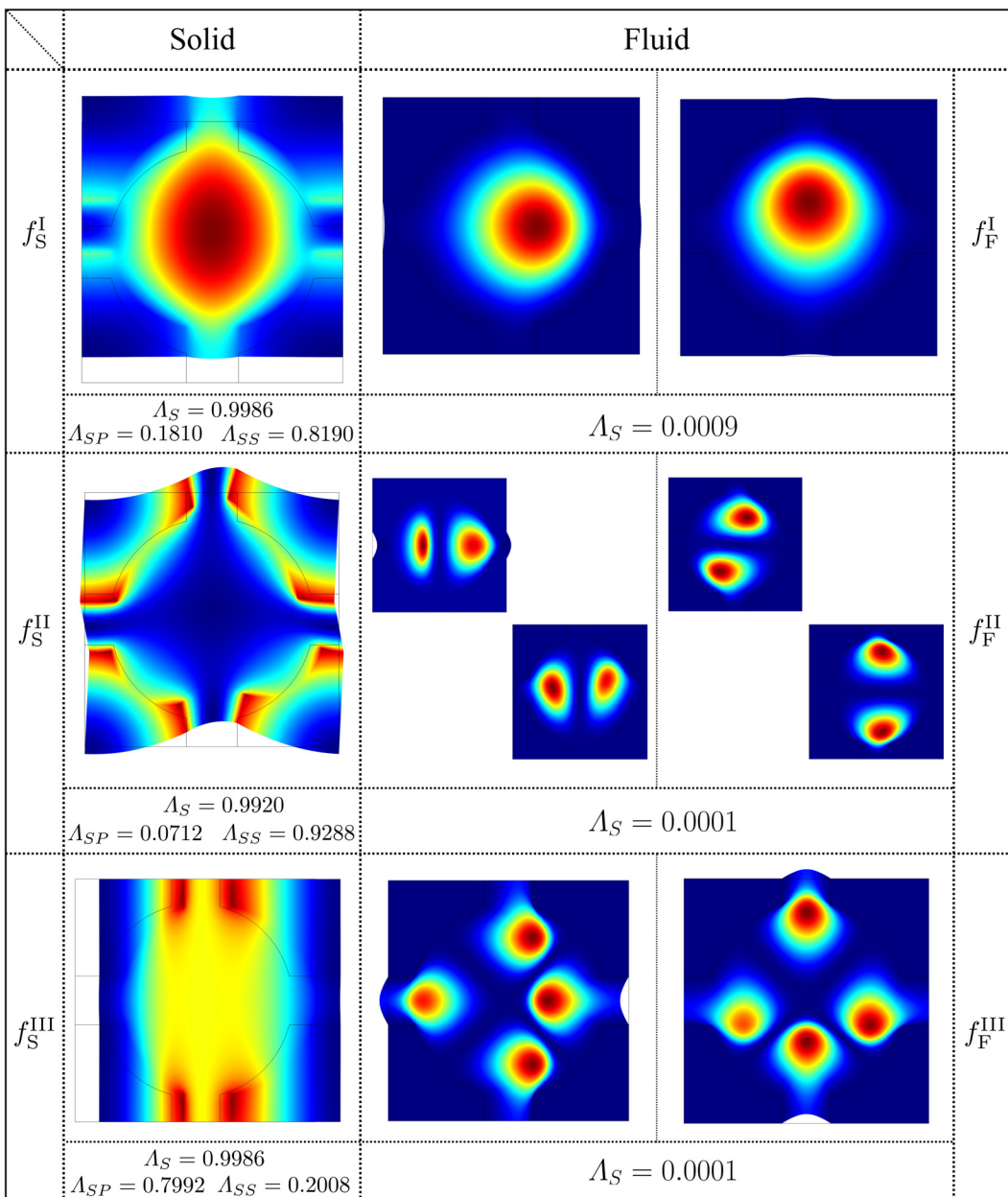


FIG. 5. (Color online) Selection of dispersion properties: polarization factor and modulus (density plots over the deformed configuration) of the waveforms associated with the lowest frequencies for reduced wavevector $c = 26.18 \text{ rad/m}$.

departing from the origin (to which f_S^I and f_S^{III} correspond) resemble the spectral properties of a classical Cauchy continuum, with the shear group velocity smaller than the pressure wave velocity. However, differently from a 2D Cauchy continuum, an extra shear waveform (to which f_S^{II} corresponds) exists. This can be observed also in higher-order continua (Parfitt and Eringen, 1966).

As a supplementary remark, it should be noted that the amplitude of bandgaps is not only a function of topology but also of geometric parameters such as r and w . These quantities could be taken as variables in an inverse design problem. A parametric study of these variables is beyond the scope of the present paper. However, some discussion on their optimal values can be found in Wang *et al.* (2023),

which ensures that the configuration considered is very close to an optimum that has bandgaps large enough without compromising the stiffness.

III. ELASTOACOUSTIC METAFILTER

Mechanical metadevices descending from periodic metamaterials have finite dimensions, for functional and manufacturing reasons as well as for guaranteeing the maximal interoperability and integrability in large engineering systems (Zheludev and Kivshar, 2012). According to this idea, the biphasic metamaterial dynamically characterized in the previous section is the conceptual background to develop a mechanical metafilter for protecting an asset

against both acoustic and elastic vibrations. From a technological perspective, the metafilter is conceived as a passive device designed to protect environments, where human well-being is a relevant issue, from the acoustic and vibrational pollution that can be generated by engines and mechanical machinery.

The mechanical metafilter is composed by a rectangular array of 11-by- N biphasic cells, where the number of columns N can be taken as a design variable. The height and width of the cellular array are $W_E = 11L$ and $D = NL$, respectively. Two different virtual experiments are conceived to assess the performance of the metafilter in impeding the propagation of acoustic and elastic waves, respectively. In the former, the metafilter is surrounded by a fluid environment (acoustic metafilter). In the latter, the metafilter is embedded into a solid environment (elastic metafilter). The environment covers two rectangular regions, with height W_E and length L_E , symmetrically placed at the two sides of the metafilter. The fluid and solid environments are made of the same materials constituting the two metafilter phases. In particular, nylon is chosen for the solid phase due to its marked additive manufacturability, accompanied by greater lightness, lower elastic moduli, and higher dissipation properties compared to printable metallic materials. A sketch of the experimental setup, which is similar to other benchmark testbeds studied in the literature (Bacigalupo *et al.*, 2020; Jin *et al.*, 2021; Montiel *et al.*, 2017; Shelke *et al.*, 2014), is reported in Fig. 6. Given the large difference of wave propagation velocities in fluid and solid materials, the environment length L_E is set to be shorter ($L_E = 0.9$ m) for the acoustic metafilter, and larger ($L_E = 2$ m) for the elastic metafilter.

A. Forced response

The metafilter performance is assessed in both time and frequency domains, based on the forced response to broadband external excitations. To this purpose, the left-end boundary of the environment region (input boundary) is forced to uniformly vibrate according to a time-history $h(t)$. The function $h(t)$ is applied as a Neumann boundary condition for both the solid and fluid environments. The time history is defined as a sine sweep signal with constant unitary amplitude, combined with two half Gaussian functions smoothing the initial (low-frequency) and final (high-frequency) parts. Specifically, the time-history law is

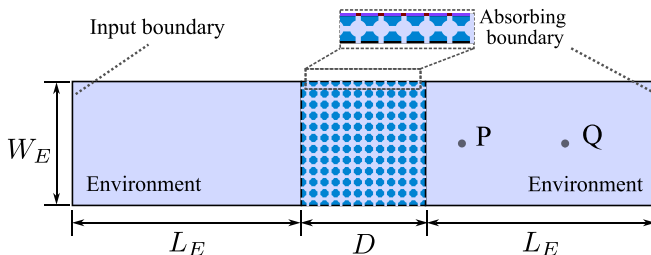


FIG. 6. (Color online) Sketch of the virtual experiment model.

$$h(t) = H(t) \sin \left[2\pi \left(f_i + \frac{\Delta f}{b} t \right) t \right], \quad (16)$$

where b is the time interval necessary to sweep from the lowest frequency f_i to the largest frequency $f_u = f_i + \Delta f$. By introducing the unit-step function $\Theta(t)$, the time-dependent multiplier $H(t)$ reads

$$\begin{aligned} H(t) = & \Theta(t - b_1) + \Theta(b_2 - t) - 1 \\ & + \Theta(b_1 - t) \exp \left(-[(b_1 - t)/(4a)]^2 \right) \\ & + \Theta(t - b_2) \exp \left(-[(b_2 - t)/(4a)]^2 \right), \end{aligned} \quad (17)$$

and accounts for the half Gaussian functions (regulated by the parameter a) before $t = b_1$ and after $t = b_2$. The time history and its Fourier transform are illustrated in Fig. 7, for $b = 4.5 \times 10^{-3}$ s, $f_i = 10$ kHz, $\Delta f = 10$ kHz, and $a = 2.44 \times 10^{-4}$ s, $b_1 = 2.8 \times 10^{-3}$ s, $b_2 = 3.7 \times 10^{-3}$ s. The forced response is investigated separately in the three frequency ranges 0–10 kHz (low, $f_i = 0$ kHz, $\Delta f = 10$ kHz), 10–20 kHz (mid, $f_i = 10$ kHz, $\Delta f = 10$ kHz), and 20–25 kHz (high, $f_i = 20$ kHz, $\Delta f = 5$ kHz).

Undesired reflections from all the other boundaries (right-end boundary and top-bottom boundaries) are prevented by defining proper acoustic and elastic absorbing boundaries, depending on the nature of the virtual experiment.

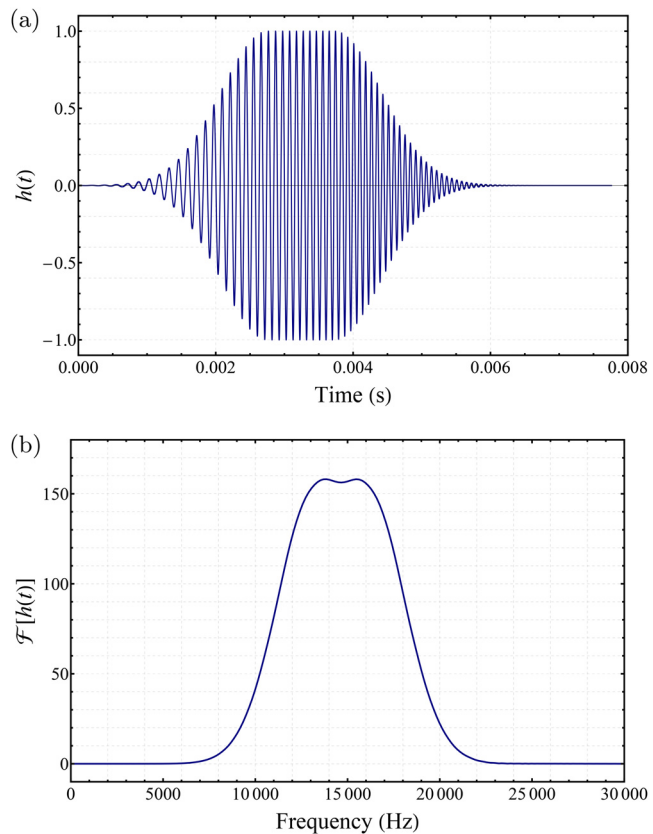


FIG. 7. (Color online) External excitation for forced response: (a) Time-history and (b) Fourier transform.

The governing equations of the acoustic absorbing boundaries are

$$\mathbf{n} \cdot \nabla u_1 = -\frac{1}{c_F} \frac{\partial u_1}{\partial t}, \quad \mathbf{n} \cdot \nabla u_2 = -\frac{1}{c_F} \frac{\partial u_2}{\partial t}, \quad (18)$$

where \mathbf{n} is the normal to the boundary. The governing equation of elastic absorbing boundaries is

$$\boldsymbol{\sigma} \mathbf{n} = -\rho_S v_S \dot{\mathbf{u}}, \quad (19)$$

where $\boldsymbol{\sigma}$ is the Cauchy stress tensor of the plane state of strain, $v_S = \sqrt{(\lambda + 2\mu)/\rho_S}$ is the longitudinal velocity of bulk pressure waves in the solid.

The broadband excitation applied to the left-end boundary initially generates a disturbance traveling from left to right. The expected behavior of the disturbance is (i) free propagation through the left environment region, (ii) impact and interaction with the mechanical metafilter, and—depending on the metafilter performance—(iii) free propagation of the unfiltered part of the disturbance through the right environment region. Therefore, two observation points (P and Q) are defined on the right-hand region (Fig. 8), to collect displacement or pressure data, disclosing qualitative and quantitative insights about the metafilter performance.

B. Transmission coefficients

The performance of the mechanical metafilter is evaluated by transmission coefficients defined on purpose, similar to the definition introduced by Ogam *et al.* (2021). Evaluating the transmission coefficients requires a comparison of the response intensity in the presence and the absence of the metafilter. Consequently, four models are analyzed and compared: (i) two biphasic models, in which the metafilter is surrounded by a fluid *or* solid environment, and (ii) two environmental-only fully fluid *or* fully solid models, without the metafilter. For each model, three analyses in different frequency ranges (*low, mid, high* ranges) are carried out separately. All the response quantities of environmental-only models (without the metafilter) are indicated by the

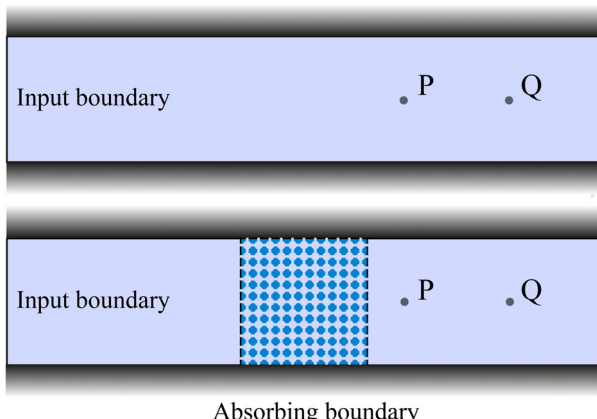


FIG. 8. (Color online) Comparison of the virtual experiment models without the metafilter (top) and with the metafilter (bottom).

superscript *. The time histories of the displacement component $u_1(t, \mathbf{x})$ and pressure $p(t, \mathbf{x})$, for the solid and fluid respectively, at two \mathbf{x} -positions, corresponding to points P and Q, are considered (Fig. 8). Therefore, the quantities T_F (*sound transmission coefficient*) and T_S (*vibration transmission coefficient*) are defined in the frequency domain on the base of the ratios,

$$[T_F(\omega, \mathbf{x})]^2 = \frac{\mathcal{P}(\omega, \mathbf{x}) \bar{\mathcal{P}}(\omega, \mathbf{x})}{\mathcal{P}^*(\omega, \mathbf{x}) \bar{\mathcal{P}}^*(\omega, \mathbf{x})}, \quad (20)$$

$$[T_S(\omega, \mathbf{x})]^2 = \frac{\mathcal{U}_1(\omega, \mathbf{x}) \bar{\mathcal{U}}_1(\omega, \mathbf{x})}{\mathcal{U}_1^*(\omega, \mathbf{x}) \bar{\mathcal{U}}_1^*(\omega, \mathbf{x})}, \quad (21)$$

where $\mathcal{P}(\omega, \mathbf{x}) = \mathcal{F}[p(t, \mathbf{x})]$ and $\mathcal{U}_1(\omega, \mathbf{x}) = \mathcal{F}[u_1(t, \mathbf{x})]$ stand for the Fourier Transforms of the pressure and displacement component, respectively. Clearly, different transmission coefficients could be introduced by considering alternative dynamic quantities, like the other component $u_2(t, \mathbf{x})$ of the displacement vector field.

The dynamic problem governing the forced response is solved according to the finite element method, by using 2D second order triangular Lagrangian elements to discretize the entire domain. Similarly to the free response problem, the maximum finite element size is not larger than 1/6 of the shortest wavelength of interest, while the solver time step is 1/20 times the smallest period (inverse of frequency) of interest. These resolutions differ in the low, mid, and high frequency ranges. For example, considering the problem concerning sound transmission, the space and time resolutions are, respectively: 5 mm and 5×10^{-6} s (low range 0–10 kHz), 2.5 mm and 2.5×10^{-6} s (mid range 10–20 kHz), and 2 mm and 2×10^{-6} s (high range 20–25 kHz).

C. Sound transmission

In the forced response simulations of sound transmission, the metafilter (with $N = 11$) is surrounded by the fluid environment. In the time domain, the propagation of sound waves from the input boundary is illustrated by intensity fields of the fluid pressure in the absence [in Fig. 9(a)] and in the presence of the metafilter [Fig. 9(b)]. Since the results are similar in the three excitation frequency ranges, only the case of broadband input signal with $f_i = 10$ kHz and $\Delta f = 10$ kHz is reported, for the sake of brevity. The pressure intensity fields are displayed in two different time instants (two in the absence and four in the presence of the metafilter). The general scenario enables one to recognize that the propagation of the plane sound wave is effectively impeded by the array of biphasic cells. This behavior is actually compatible with the structure of the dispersion curves, which presents a stopband in the frequency range of the input signal. An enlargement of the pressure field in the vicinity of the left metafilter boundary [Fig. 9(c)] discloses the filtering mechanism: the sound wave is trapped within a limited number of cells close to the boundary. Moreover, the pressure field within these cells closely resembles that of the second fluid waveform (at frequency $f_F^{II} \simeq 17$ kHz), reported

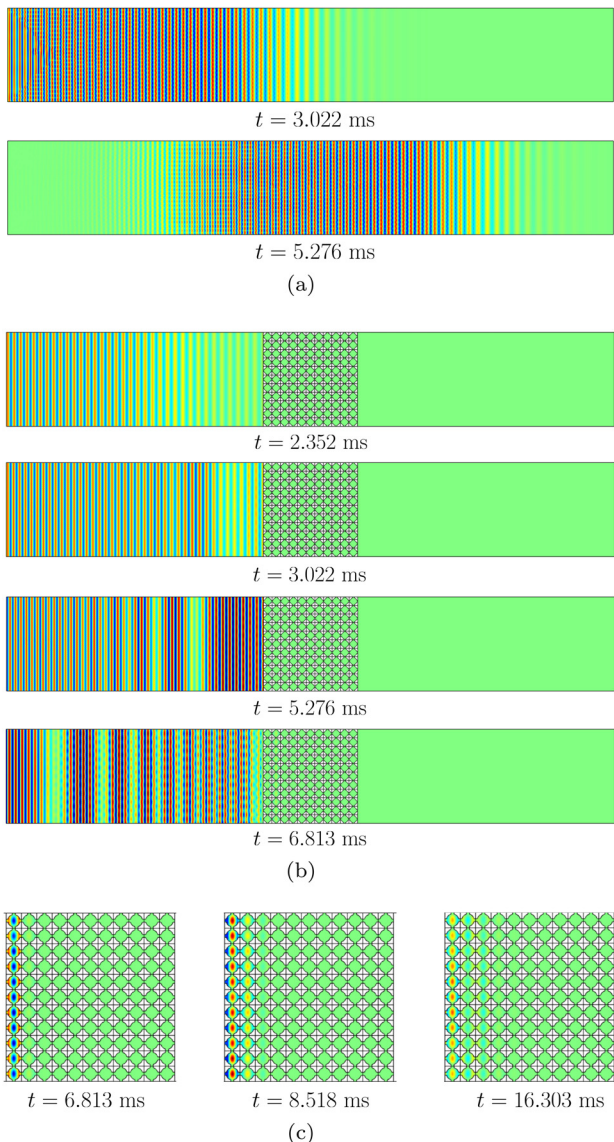


FIG. 9. (Color online) Forced response (pressure field) of the fluid environment to broad input signal ($f_i = 10$ kHz and $\Delta f = 10$ kHz) at different time instants: (a) without acoustic metafilter, and (b) with acoustic metafilter.

in Fig. 10. In fact, it should be noted that this waveform is associated with the second flatband, which has negligible group velocity. In such a case, all the waveforms belonging to the flatband can propagate spatially with opposite wave vectors, with the same phase velocity, without any energy transfer. In an infinite metafilter, with a continuous feed of energy from a monoharmonic excitation, this would result in a stationary vibration field. Given the finiteness of the metafilter and the broadband nature of the excitation, a spatially-localized vibration field with a modest amount of transmission occurs.

In the frequency domain, the propagation of sound waves from the input boundary is illustrated by the transmission coefficient of points P and Q, which are located at a distance of 0.2 m and 0.5 m from the right boundary of the metafilter, respectively. First, it should be noted that these points exhibit quite similar results in terms of transmission

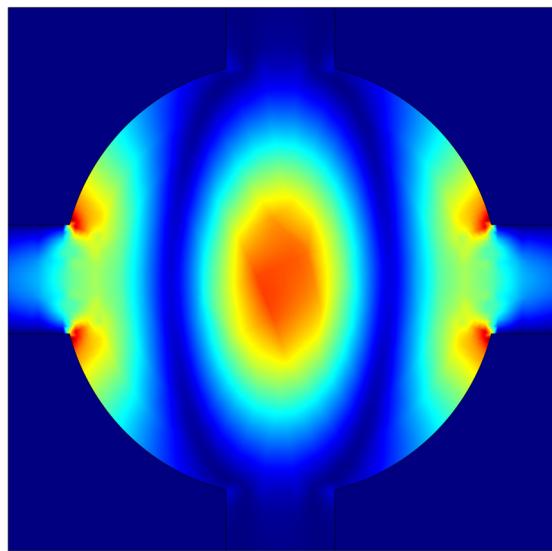


FIG. 10. (Color online) Pressure field of the waveform associated with f_F^{II} .

coefficients, mainly due to the absence of damping. For the sake of brevity, only results pertaining to point P are discussed. The results obtained are displayed in Fig. 11, where the transmission coefficient T_F (red curve) is reported in dB as a function of frequency within the low, mid, and high frequency ranges of the excitations. The dispersion diagram (black dots) is superimposed on the transmission coefficient to ease the result interpretation.

In all the excitation frequency ranges, there is a strong dependence of the transmission coefficients on the frequency and marked levels of reduction of the transmitted response, especially within the stopbands. In the low frequency range [0–10 kHz, see Fig. 11(a)], the largest values of the sound transmission coefficient T_F are located in the 0–3 kHz band, coinciding with the low-frequency elastic passband of the dispersion diagram. In fact, in the presence of solid dispersion curves acoustic wave propagation is allowed, due to the solid/fluid interaction.

In the mid frequency range [10–20 kHz, see Fig. 11(b)], two flatbands exist around 11 kHz and 17 kHz. At these frequencies, the coefficient T_F is expected to increase slightly, coherently with the remarks highlighted in the discussion of the time domain analyses. In fact, a sharp peak clearly appears around 17 kHz. The peak at 11 kHz is actually present, but much less pronounced because this frequency falls at the beginning of the excitation broadband and therefore is excited with a lower amount of energy. Moreover, given that the external excitation generates a plane wavefront, it is apparent that the first waveform receives a smaller amount of energy compared with the second, depending on their respective shapes reported in Fig. 5.

In the high frequency range [20–25 kHz, see Fig. 11(c)], several acoustic dispersion curves densely coexist in the dispersion diagram, especially for frequencies larger than 22 kHz. From the qualitative viewpoint, the transmission coefficient is coherent with this condition of high spectral density, showing several local and global peaks in the

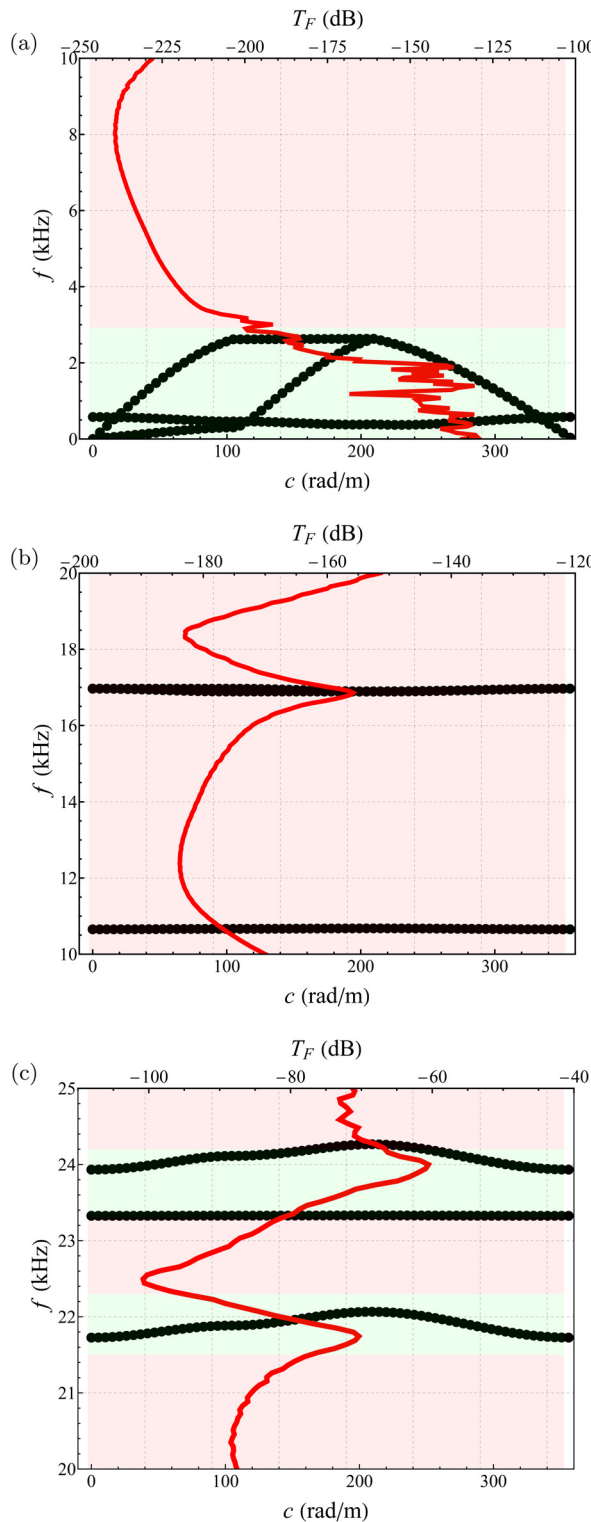


FIG. 11. (Color online) Sound transmission coefficient in the frequency range of (a) 0–10 kHz, (b) 10–20 kHz, (c) 20–25 kHz.

general context of high values. Indeed, from the quantitative viewpoint, in this frequency band, the transmission coefficient attains the largest values among the three frequency ranges considered.

Overall, the finite element analyses provide evidence that the virtual experimental behavior of the metafilter is

consistent with the dispersion curves of the mechanical metamaterial, that is, sound waves tend to be passively attenuated more efficiently within bandgaps. In all the frequency ranges analyzed, very strong amplitude reduction was achieved, despite the occurrence of narrow peaks corresponding to the quasi flatbands.

D. Vibration transmission

In the forced response simulations for the analysis of transmission of elastic vibrations, the metafilter ($N=11$) is surrounded by a solid environment. Points P and Q are located at a distance of 0.5 m and 1 m from the right boundary of the metafilter. Similar to what was observed with sound transmission, these points exhibit quite similar responses in terms of transmission coefficients. The propagation of elastic waves from the input boundary is first illustrated in the time domain by the modulus of the displacement field in the absence [at two time instants in Fig. 12(a)] and in the presence [at two time instants in Fig. 12(b)] of the metafilter. Given the similarity of the results in the three frequency ranges of the input signals under study, only the response to a broadband input signal with $f_i=10$ kHz and $\Delta f=10$ kHz is reported. From the comparison of the results, it can be recognized that the elastic disturbance originated by the external excitation does not penetrate into the metafilter, but is trapped within the first column of cells. This behavior is actually compatible with the structure of the dispersion curves, which present a complete stopband in the frequency range of the excitation.

The vibration transmission coefficients are reported in red in Fig. 13, with superimposition of the dispersion curves (black dots) to discuss the results in the frequency domain. It can be observed that, similarly to the sound transmission, the metafilter provides a strong attenuation within the stopbands. Specifically, the largest values of the vibration transmission are attained within the low-frequency range, in the passband of the elastic dispersion curves (0–3 kHz). In the

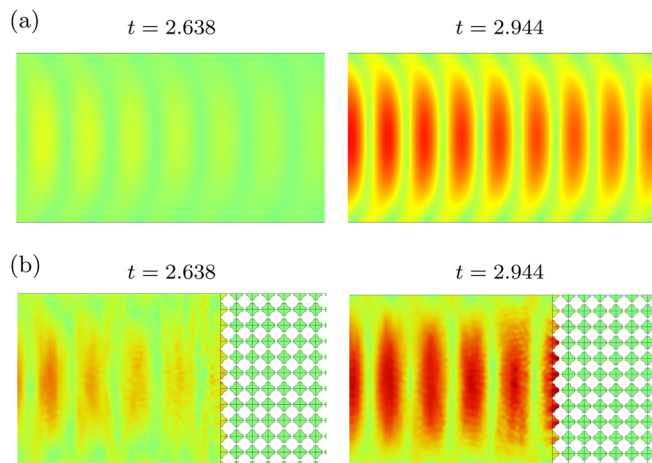


FIG. 12. (Color online) Forced response of the solid environment to broad input signal ($f_i=10$ kHz and $\Delta f=10$ kHz) at different time instants: (a) without elastic metafilter at 2 m distance from the input boundary, and (b) with elastic metafilter.

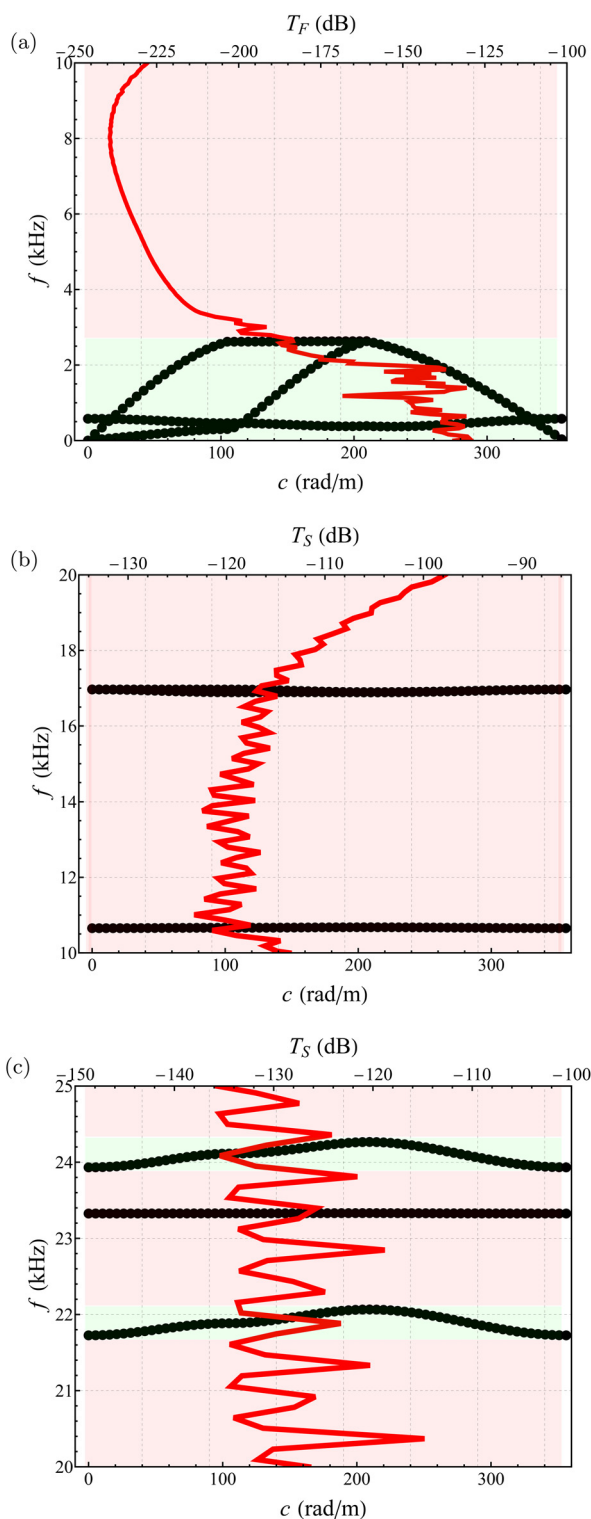


FIG. 13. (Color online) Vibration transmission coefficient in the frequency range of: (a) 0–10 kHz, (b) 10–20 kHz, (c) 20–25 kHz.

mid frequency range, the transmission coefficient is very small, by virtue of the complete bandgap, interrupted only by acoustic flatbands. No clear peaks are observable in correspondence with flatbands, as expected. In the high frequency band, the transmission coefficient is the smallest of all the three frequency bands investigated. It can be

concluded that, in the case of vibration transmission, the presence of acoustic dispersion curves has negligible influence on transmission. It is worth remarking that using a vibration transmission coefficient based on the displacement component $u_2(t, \mathbf{x})$ provides similar results, which are not reported here for the sake of brevity.

IV. CONCLUSIONS

In this paper, the free propagation of sound and elastic waves in a biphasic 2D mechanical metamaterial is investigated. The mechanical metamaterial is developed starting from a high-contrast phononic crystal, by enriching the microstructure of a periodic arrangement of square solid cells, each hosting a circular fluid-filled cavity. The periodicity-preserving microstructuring consists of opening intercellular channels to connect all the regions occupied by the fluid phase while adding channel-bridging deformable connections to elastically couple the adjacent regions made of the solid phase. The linear partial differential equations governing the free undamped response of the solid and fluid domains—equipped by consistent coupling conditions at the interfaces—have been solved using a hybrid analytical-computational technique that exploits the periodicity to determine the dispersion properties. The intercellular channels and channel-bridging connections have been verified to, first, strongly reduce the low-frequency pass bandwidth characterizing the phononic crystal, and, second, open bandgaps with large bandwidths in the dispersion diagram. Specifically, complete bandgaps have been obtained in a considerable fraction of the frequency range 0–25 kHz, which is of utmost theoretical and practical interest, since it is the frequency band of human sensitivity to sound and vibration. For the dispersion curves defining the passbands of the metamaterials spectrum, the waveforms have been classified on the base of their polarization, depending on the kinetic energy stored in the fluid or the solid phase. The classification has allowed us to distinguish elastic from acoustic waveforms, which have been found to dwell in the low-frequency band (0–3 kHz) and the high-frequency band (higher than 22 kHz), respectively. A secondary sub-classification, based on the elastic energy stored in the solid phase, has enabled one to recognize elastic waveforms dominated by shear and normal strains.

In addition, computational investigations have been performed to analyze the forced response of an array of a finite number of metamaterial cells. This cellular system has demonstrated its ability to impede the propagation of both acoustic and elastic vibration. In particular, a remarkable reduction of the transmitted response has been achieved in the frequency band of human sensitivity to sound and vibration. The protection properties against both acoustic and elastic vibrations pave the way to design devices working as passive mechanical metafilters that can be profitably used in practical applications.

ACKNOWLEDGMENTS

This study was carried out within the MOST—Sustainable Mobility National Research Center. M.W.

received funding from the European Union Next-GenerationEU (PIANO NAZIONALE DI RIPRESA E RESILIENZA (PNRR)—MISSIONE 4 COMPONENTE 2, INVESTIMENTO 1.4—D.D. 1033 17/06/2022, CN00000023). The funding contribution from the National Center on HPC, Big Data and Quantum Computing CN00000013 is also gratefully acknowledged by A.P. This manuscript reflects only the authors' views and opinions, neither the European Union nor the European Commission can be considered responsible for them.

AUTHOR DECLARATIONS

Conflict of Interest

The authors declare no conflicts of interest.

DATA AVAILABILITY

The data that support the findings of this study are available from the corresponding author upon reasonable request.

- Bacigalupo, A., De Bellis, M. L., and Misseroni, D. (2020). "Design of tunable acoustic metamaterials with periodic piezoelectric microstructure," *Extreme Mech. Lett.* **40**, 100977.
- Bacigalupo, A., Gnecco, G., Lepidi, M., and Gambarotta, L. (2021). "Computational design of innovative mechanical metafilters via adaptive surrogate-based optimization," *Comput. Methods Appl. Mech. Eng.* **375**, 113623.
- Bacigalupo, A., and Lepidi, M. (2018). "Acoustic wave polarization and energy flow in periodic beam lattice materials," *Int. J. Solids Struct.* **147**, 183–203.
- Bilal, O. R., Ballagi, D., and Daraio, C. (2018). "Architected lattices for simultaneous broadband attenuation of airborne sound and mechanical vibrations in all directions," *Phys. Rev. Appl.* **10**(5), 054060.
- Bilal, O. R., and Hussein, M. I. (2011). "Ultrawide phononic band gap for combined in-plane and out-of-plane waves," *Phys. Rev. E* **84**(6), 065701.
- Chen, Y., Lan, Z., Su, Z., and Zhu, J. (2022). "Inverse design of photonic and phononic topological insulators: A review," *Nanophotonics* **11**(19), 4347–4362.
- Chen, Y., Meng, F., Sun, G., Li, G., and Huang, X. (2017). "Topological design of phononic crystals for unidirectional acoustic transmission," *J. Sound Vib.* **410**, 103–123.
- Claeys, C. C., Vergote, K., Sas, P., and Desmet, W. (2013). "On the potential of tuned resonators to obtain low-frequency vibrational stop bands in periodic panels," *J. Sound Vib.* **332**(6), 1418–1436.
- Cummer, S. A., Christensen, J., and Alù, A. (2016). "Controlling sound with acoustic metamaterials," *Nat. Rev. Mater.* **1**(3), 16001.
- D'Alessandro, L., Zega, V., Ardito, R., and Corigliano, A. (2018). "3D auxetic single material periodic structure with ultra-wide tunable bandgap," *Sci. Rep.* **8**(1), 2262.
- Delpero, T., Schoenwald, S., Zemp, A., and Bergamini, A. (2016). "Structural engineering of three-dimensional phononic crystals," *J. Sound Vib.* **363**, 156–165.
- Elmadih, W., Chronopoulos, D., and Zhu, J. (2021). "Metamaterials for simultaneous acoustic and elastic bandgaps," *Sci. Rep.* **11**(1), 14635.
- Faraci, D., Comi, C., and Marigo, J.-J. (2022). "Band gaps in metamaterial plates: Asymptotic homogenization and bloch-floquet approaches," *J. Elast.* **148**(1), 55–79.
- Frazier, M. J., and Hussein, M. I. (2015). "Viscous-to-viscoelastic transition in phononic crystal and metamaterial band structures," *J. Acoust. Soc. Am.* **138**(5), 3169–3180.
- Gao, J., Cao, X., Xiao, M., Yang, Z., Zhou, X., Li, Y., Gao, L., Yan, W., Rabczuk, T., and Mai, Y.-W. (2023). "Rational designs of mechanical metamaterials: Formulations, architectures, tessellations and prospects," *Mater. Sci. Eng.: R: Rep.* **156**, 100755.

- Gao, N., Zhang, Z., Deng, J., Guo, X., Cheng, B., and Hou, H. (2022). "Acoustic metamaterials for noise reduction: A review," *Adv. Mater. Technol.* **7**(6), 2100698.
- Gattulli, V., and Lepidi, M. (2007). "Localization and veering in the dynamics of cable-stayed bridges," *Comput. Struct.* **85**(21–22), 1661–1678.
- Goffaux, C., and Vigneron, J. (2001). "Theoretical study of a tunable phononic band gap system," *Phys. Rev. B* **64**(7), 075118.
- Hagedorn, P., and DasGupta, A. (2007). *Vibrations and Waves in Continuous Mechanical Systems* (John Wiley & Sons, New York).
- Hakoda, C., Rose, J., Shokouhi, P., and Lissenden, C. (2018). "Using Floquet periodicity to easily calculate dispersion curves and wave structures of homogeneous waveguides," *AIP Conf. Proc.* **1949**, 020016.
- Hou, Z., Fu, X., and Liu, Y. (2006). "Singularity of the Bloch theorem in the fluid/solid phononic crystal," *Phys. Rev. B* **73**(2), 024304.
- Hussein, M. I., and Frazier, M. J. (2010). "Band structure of phononic crystals with general damping," *J. Appl. Phys.* **108**(9), 093506.
- Hussein, M. I., Leamy, M. J., and Ruzzene, M. (2014). "Dynamics of phononic materials and structures: Historical origins, recent progress, and future outlook," *Appl. Mech. Rev.* **66**(4), 040802.
- Jiang, H., and Chen, Y. (2019). "Lightweight architected hollow sphere foams for simultaneous noise and vibration control," *J. Phys. D: Appl. Phys.* **52**(32), 325303.
- Jin, Y., Pennec, Y., Bonello, B., Honarvar, H., Dobrzynski, L., Djafari-Rouhani, B., and Hussein, M. I. (2021). "Physics of surface vibrational resonances: Pillared phononic crystals, metamaterials, and metasurfaces," *Rep. Prog. Phys.* **84**(8), 086502.
- Krushynska, A. O., Torrent, D., Aragón, A. M., Ardito, R., Bilal, O. R., Bonello, B., Bosia, F., Chen, Y., Christensen, J., Colombi, A., Cummer, S. A., Djafari-Rouhani, B., Fraternaili, F., Galich, P., Garcia, P. D., Groby, J.-P., Guenneau, S., Haberman, M. R., Hussein, S., Jambaz, N., Jimenez, N., Khelif, A., Laude, V., Mirzaali, M., Packo, P., Palermo, A., Pennec, Y., Pico, R., Lopez, M. R., Rudykh, S., Serra-Garcia, M., Torres, C. M., Starkey, T. A., Tourant, V., and Wright, O. B. (2023). "Emerging topics in nanophononics and elastic, acoustic, and mechanical metamaterials: An overview," *Nanophotonics* **12**(4), 659–686.
- Laude, V. (2020). *Phononic Crystals: Artificial Crystals for Sonic, Acoustic, and Elastic Waves* (Walter de Gruyter GmbH & Co KG, Berlin).
- Lepidi, M., and Bacigalupo, A. (2018). "Multi-parametric sensitivity analysis of the band structure for tetrachiral acoustic metamaterials," *Int. J. Solids Struct.* **136–137**, 186–202.
- Li, E., He, Z., Wang, G., and Liu, G. (2018). "An efficient algorithm to analyze wave propagation in fluid/solid and solid/fluid phononic crystals," *Comput. Methods Appl. Mech. Eng.* **333**, 421–442.
- Li, F.-L., Wang, Y.-S., and Zhang, C. (2011). "Bandgap calculation of two-dimensional mixed solid-fluid phononic crystals by Dirichlet-to-Neumann maps," *Phys. Scr.* **84**(5), 055402.
- Li, J., Wen, X., and Sheng, P. (2021). "Acoustic metamaterials," *J. Appl. Phys.* **129**(17), 171103.
- Liu, Z., Zhang, X., Mao, Y., Zhu, Y., Yang, Z., Chan, C. T., and Sheng, P. (2000). "Locally resonant sonic materials," *Science* **289**(5485), 1734–1736.
- Ma, G., and Sheng, P. (2016). "Acoustic metamaterials: From local resonances to broad horizons," *Sci. Adv.* **2**(2), e1501595.
- Maldovan, M. (2013). "Sound and heat revolutions in phononics," *Nature* **503**(7475), 209–217.
- Martínez-Sala, R., Sancho, J., Sánchez, J. V., Gómez, V., Llinares, J., and Mesequer, F. (1995). "Sound attenuation by sculpture," *Nature* **378**(6554), 241–241.
- Marzani, A., Viola, E., Bartoli, I., Lanza di Scalea, F., and Rizzo, P. (2008). "A semi-analytical finite element formulation for modeling stress wave propagation in axisymmetric damped waveguides," *J. Sound Vib.* **318**(3), 488–505.
- Maurin, F., Claeys, C., Deckers, E., and Desmet, W. (2018). "Probability that a band-gap extremum is located on the irreducible Brillouin-zone contour for the 17 different plane crystallographic lattices," *Int. J. Solids Struct.* **135**, 26–36.
- McGurn, A. (2022). *Synthesis Lectures on Materials and Optics: Introduction to Photonic and Phononic Crystals and Metamaterials* (Springer International Publishing, New York).

- Montiel, F., Chung, H., Karimi, M., and Kessissoglou, N. (2017). "An analytical and numerical investigation of acoustic attenuation by a finite sonic crystal," *Wave Motion* **70**, 135–151.
- Ogam, E., El Abbidine Fellah, Z., Fellah, M., and Depollier, C. (2021). "Theoretical and experimental study of micropolar elastic materials using acoustic waves in air," *J. Sound Vib.* **510**, 116298.
- Oudich, M., Gerard, N. J., Deng, Y., and Jing, Y. (2023). "Tailoring structure-borne sound through bandgap engineering in phononic crystals and metamaterials: A comprehensive review," *Adv. Funct. Mater.* **33**(2), 2206309.
- Parfitt, V., and Eringen, A. (1966). "Reflection of plane waves from the flat boundary of a micropolar elastic half-space," *J. Acoust. Soc. Am.* **45**(5), 1258–1272.
- Patil, G. U., Cui, S., and Matlack, K. H. (2022). "Leveraging nonlinear wave mixing in rough contacts-based phononic diodes for tunable nonreciprocal waves," *Extreme Mech. Lett.* **55**, 101821.
- Pau, A., and Lanza Di Scalea, F. (2015). "Nonlinear guided wave propagation in prestressed plates," *J. Acoust. Soc. Am.* **137**(3), 1529–1540.
- Pau, A., and Trovalusci, P. (2021). "A multifield continuum model for the description of the response of microporous/microcracked composite materials," *Mech. Mater.* **160**, 103965.
- Romero-García, V., Sánchez-Pérez, J. V., García-Raffi, L. M., Herrero, J., García-Nieto, S., and Blasco, X. (2009). "Hole distribution in phononic crystals: Design and optimization," *J. Acoust. Soc. Am.* **125**(6), 3774–3783.
- Sharma, G. S., Skvortsov, A., MacGillivray, I., and Kessissoglou, N. (2017). "Sound transmission through a periodically voided soft elastic medium submerged in water," *Wave Motion* **70**, 101–112.
- Shelke, A., Banerjee, S., Habib, A., Rahani, E. K., Ahmed, R., and Kundu, T. (2014). "Wave guiding and wave modulation using phononic crystal defects," *J. Intell. Mater. Syst. Struct.* **25**(13), 1541–1552.
- Sigalas, M. M. (1992). "Elastic and acoustic wave band structure," *J. Sound Vib.* **158**(2), 377–382.
- Tanaka, Y., Tomoyasu, Y., and Tamura, S.-I. (2000). "Band structure of acoustic waves in phononic lattices: Two-dimensional composites with large acoustic mismatch," *Phys. Rev. B* **62**(11), 7387.
- Vasseur, J. O., Deymier, P., Khelif, A., Lambin, P., Djafari-Rouhani, B., Akjouj, A., Dobrzynski, L., Fettouhi, N., and Zemmouri, J. (2002). "Phononic crystal with low filling fraction and absolute acoustic band gap in the audible frequency range: A theoretical and experimental study," *Phys. Rev. E* **65**(5), 056608.
- Wang, M., Pau, A., and Lepidi, M. (2023). "Design of mechanical metamaterials based on biphasic periodic microstructure," in *Proceedings of the 10th ECCOMAS Thematic Conference on Smart Structures and Materials, SMART 2023*, July 3–5, Patras, Greece.
- Wang, Y.-F., Wang, Y.-Z., Wu, B., Chen, W., and Wang, Y.-S. (2020a). "Tunable and active phononic crystals and metamaterials," *Appl. Mech. Rev.* **72**(4), 040801.
- Wang, Y.-F., Zhang, S.-Y., Wang, Y.-S., and Laude, V. (2020b). "Hybridization of resonant modes and bloch waves in acoustoelastic phononic crystals," *Phys. Rev. B* **102**(14), 144303.
- Zangeneh-Nejad, F., and Fleury, R. (2019). "Active times for acoustic metamaterials," *Rev. Phys.* **4**, 100031.
- Zega, V., Pertoldi, L., Zandrini, T., Osellame, R., Comi, C., and Corigliano, A. (2022). "Microstructured phononic crystal isolates from ultrasonic mechanical vibrations," *Appl. Sci.* **12**(5), 2499.
- Zhang, J., Hu, B., and Wang, S. (2023). "Review and perspective on acoustic metamaterials: From fundamentals to applications," *Appl. Phys. Lett.* **123**(1), 010502.
- Zhao, H., Wen, J., Yu, D., and Wen, X. (2010). "Low-frequency acoustic absorption of localized resonances: Experiment and theory," *J. Appl. Phys.* **107**(2), 023519.
- Zheludev, N. I., and Kivshar, Y. S. (2012). "From metamaterials to meta-devices," *Nat. Mater.* **11**(11), 917–924.